Journal of the European Ceramic Society 40 (2020) 2691–2698
https://doi.org/10.1016/j.jeurceramsoc.2019.12.038
Submitted 16 July 2019

Off-axis damage tolerance of fiber-reinforced composites for aerospace systems

P. Galizia*, L. Zoli, F. Saraga and D. Sciti

CNR-ISTEC, National Research Council of Italy - Institute of Science and Technology for Ceramics, Via Granarolo 64, Faenza, I-48018

*corresponding author, e-mail: pietro.galizia@istec.cnr.it

Abstract

Strength retention of continuous carbon fiber-reinforced dense ZrB_2-based ceramics (C_f/ZrB_2) after thermal or indentation damage was evaluated. Thermal damage was *in-situ* induced and characterized by cyclic dilatometric analysis. Indentation damage was induced through Vickers indentation and then characterized by digital microscopy. The investigation of Vickers imprints figured out that residual stresses promote the material pileup and the appearance of out-of-plane freed fibers (*OFF*) onto the fibers' plane and out-of-fibers' plane, respectively. On the other hand, thermal damage reduces the residual stresses and leaves inner freed fibers (*IFF*) which enhance the elastic response. Finally, the flexural tests on damaged specimens unexpectedly revealed that C_f/ZrB_2 kept its load bearing capability in both cases and showed damage insensitivity although tested in fully matrix-dominated loading configuration (off-axis configuration).

Keywords: transverse direction; anisotropic porous ZrB_2; continuous fiber ceramic composites (CFCC); Vickers indentation; pile-up.

1 Introduction

Ultra-high temperature ceramic matrix composites (*UHTCMCs*) are currently attracting increasing research interest for their potential impact in the aerospace field [1,2]. With respect to the already used C/SiC composites for nose cones, leading edges and rocket nozzles, *UHTCMCs* promise to increase the operating limit from ~1600°C to above 2000°C while keeping good structural behaviour, dimensional tolerances and thermal shock resistance [1,3]. *UHTCMCs* are based on a dense-matrix of borides, carbides or nitrides such as ZrB_2, HfB_2, ZrC, HfC, TaC, HfN, and carbon fiber reinforcement (C_f). The former is characterized by high melting points, high hardness, chemical inertness and relatively good resistance to oxidation in severe environments [4-7]. The latter should enhance the damage tolerance and shock resistance [8]. From 2015, the properties of the "baseline *UHTCMC*" based on ZrB_2 matrix reinforced with unidirectional 45 vol% of high-modulus carbon fiber have been greatly improved, and are showing a considerable margin for further development in terms of structural properties, oxidation and ablation resistance [9-12]. Nowadays, the flexural strength at RT and 1500 °C, and the fracture toughness are around *360 MPa*, *550 MPa*, and *11 MPa·m$^{1/2}$*, respectively [1,13], compared to the preliminary values of these composite series, *260 MPa* and *200 MPa*, respectively, at *RT* and *1800 °C* [14]. The composites science agrees that flaw-tolerant ceramic-matrix composites can be developed by deliberately inducing delamination modes (i.e. *H*-crack formation). Basically, flaw-tolerant behaviour is promoted by designing matrix pore structures (i.e. porous-matrix continuous-fiber-reinforced ceramic composites, *CFCCs*), or by designing the weakness of the matrix/fiber interfaces (*i.e.* dense-matrix *CFCCs* with weak interphases) [15,16]. A porosity higher than 10 % could jeopardize ablation, erosion and oxidation resistance, and off-axis strength. On the other hand, it is not easy to obtain dense-*UHTC* matrix *CFCCs* with weak interphases. A good strategy to achieve weak interfaces is grouping the fibers into bundles in order to exploit the weak C_f/C_f and C_f/ZrB_2 interfaces within the bundles [13]. Anyway, this architecture, also called "salami-inspired" or "non-periodic", reduces the off-axis strength and is suspected to decrease ablation and oxidation resistance with respect to the corresponding periodic structures [5].

In this work, we showed that sintered *UHTC* matrix, with just 7% of residual porosity and reinforced with strongly bonded continuous fibers, is unaffected by thermal damage and indentation. Hence, it is possible to maximize the off-axis strength without compromising the damage-tolerant characteristic as consequence of the "excessive" sintering and strong matrix/fiber interfaces. The supporting results are based on (i) the investigation of the thermal and indentation damage by dilatometric analysis and optical investigation of the indentation imprints, respectively, both along transverse direction (*TD*) and longitudinal direction (*LD*); (ii) off-axis strength retention after damage induced by thermal cycling or indentation. Since *TD* avoids the reinforcement effect of the fiber, during the bending test this configuration ensures a valid failure under tensile stress without any interlaminar shear incoming. By suppressing the delamination mode, it was guaranteed that the observed flaw-tolerant did not depend on the applied stress and was not deliberately induced [15]. Furthermore, since the fibers were perpendicular to the applied tensile stress, they were not the reason of the damage insensitivity as generally observed in *CMCs* where fibres in the damage zone are subjected to stresses that are comparable in magnitude to the remote stresses [17-19].

2 Materials and methods

2.1 Material manufacturing and microstructure characterization

UHTCMCs based on carbon fiber-reinforced ZrB_2 were produced by hot pressing at *1900°C*. The final microstructure consists in *55 vol%* of matrix (*83 %* ZrB_2 + *10 vol%* SiC + *7 %* pores) and *45 vol%* C_f. Further details on slurry preparation, infiltration, densification, and microstructural and mechanical features of the produced samples were reported in a previously published work [1].

The microstructure was analyzed on polished and fractured surfaces by field emission scanning electron microscopy (*FE-SEM*, Carl Zeiss ΣIGMA NTS Gmbh Öberkochen, Germany). Bars for thermal and mechanical characterization were machined both in the longitudinal and transverse direction, here forth indicated as AP-$ZrB_2/C_{f,L}$,*AP-* $ZrB_2/C_{f,T,}$ respectively.

2.2 Dilatometric analysis

For thermal damage determination, 5 consecutive cycles from room temperature up to 1300°C were carried out using a dilatometer (Netzsch mod. DIL E 402, Germany), on *25 mm x 2.5 mm x 2 mm bars* (Fig.1 (a)), under flowing argon, 10°C/min heating rate. The relative dimensional change ($\Delta L/L_0$) *vs.* temperature was recorded both along *TD* (sample named *TC-*$ZrB_2/C_{f,T}$) and *LD* (sample named *TC-*$ZrB_2/C_{f,L}$) . The coefficient of thermal expansion (*CTE*) was measured from the slope of the secant line joining the values at *25 °C* and *1300 °C*. After 5 cycles, *TD* and *LD* bars were also indented as explained below.

2.3 Indentation analysis

10 and 20 Kg indentations were introduced by using a Vickers diamond pyramid indenter (Innovatest Falcon 500, Netherlands), in air as explained below.

a) In order to study the indentation damage, 3 Vickers indentations with a *10 kg load* were applied on *25x2.5* and *25x2* mm^2 surfaces (fiber's plane and out-of-fiber's plane, respectively, see Fig.1 (b)) of both as produced composites (*AP-*$ZrB_2/C_{f,T}$ and *AP-*$ZrB_2/C_{f,L}$, respectively) and thermally cycled composites (*TC-*$ZrB_2/C_{f,T}$ and *TC-*$ZrB_2/C_{f,L}$, respectively) . One of the diagonals of each of the indentations was aligned parallel to the test specimen length. The indentations were characterized through *SEM* and digital microscopy (HIROX RH 2000, Japan). From the obtained *3D* reconstruction of the imprints, the indentation profiles along the two diagonals were extrapolated.

b) A load of *20 kg* was applied to *25x2.5* mm^2 tensile surface of *AP-*$ZrB_2/C_{f,T}$ specimens (Fig.1 (c)), which then were mechanically tested as described in the following (*I-*$ZrB_2/C_{f,T}$ specimens). We chose to apply an higher indentation load to *I-*$ZrB_2/C_{f,T}$ specimens in order to mechanically test the beams with a damage size as large as possible. The indentation load of *20 kg* was decreased down to *10 kg* in order to avoid the break under indentation of *TC*.

2.4 Bending test

4-point flexural strength (σ) was measured at room temperature on specimens with dimensions of *25×2.5×2 mm*^{3} (length × width × thickness), lower span of *20 mm* and an upper span of *10 mm* using a Zwick-Roell Z050 testing machine. The crosshead speed was fixed to *1 mm/min*. Three bars for each kind of specimen were tested:

- as produced composite, labelled as *AP-*$ZrB_2/C_{f,T}$;
- thermally cycled composite with the above dilatometric analysis, labelled as *TC-*$ZrB_2/C_{f,T}$;
- intended composite, labelled as *I-*$ZrB_2/C_{f,T}$.

T subscript means that all the bars were tested with the fiber aligned transversally to the tensile stress, as shown in the sketch (Fig.1 (c)). It worth noticing that specimen geometry and bending test configuration were chosen in order to avoid the shear failure, and to ensure that fracture occurs in a tensile mode, i.e. transverse tensile failure. The conditions were identified through a comparison of the maximum values of tensile (σ_t) and shear (τ_i) stress achieved during the bending test and the critical values of these stresses needed to initiate tensile and shear failure, $\sigma_{t,c}$ *= 63 ± 7 MPa* and $\tau_{i,c}$ *= 36 ± 4 MPa*, respectively [1]. The resulting condition to avoid the shear failure is:

$$\frac{\tau_{i,c}}{\sigma_{t,c}} > \frac{t}{s} \qquad (1)$$

Hence the present conditions: $\tau_{i,c}/\sigma_{t,c}$ and *t/s = 2/20* (thickness-to-lower span ratio), widely satisfy the Eq.(1), at least for the *AP-*$ZrB_2/C_{f,T}$ bars.

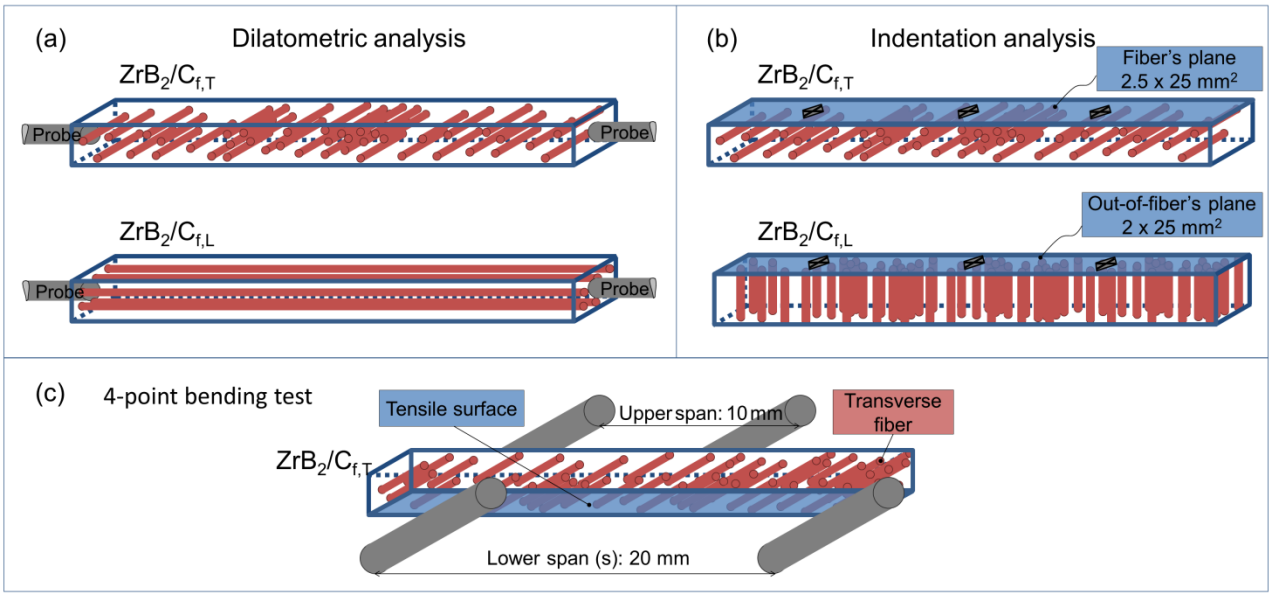

Fig.1 Sketch of the composites configuration for the (a) dilatrometric analysis, where probes push the *2.5x2 mm²* surfaces for both transversal and longitudinal fiber configurations: $ZrB_2/C_{f,T}$, and $ZrB_2/C_{f,L}$, respectively. (b) *10 kg* Vickers indentation: 3 indentations were done on the *25x2.5 mm²* surface (fiber's plane) or *25x2 mm²* surface (out-of-fiber's plane) for $ZrB_2/C_{f,T}$ and $ZrB_2/C_{f,L}$, respectively, and in both material states: as-produced (*AP*) and thermally cycled (*TC*). (c) *4*-point bending test was performed in the transversal configuration for *AP*, *TC* and *20 kg* Vickers indented specimens. All the beams with dimensions of *25×2.5×2 mm³* (length × width × thickness) were drawn with isometric cavalier perspective (angle between *x*- and *z*-axis is *150°* for (a) and (b), and *255°* for (c)).

3 Results and discussion

3.1 Microstructure

Fig.2 shows the typical interface between matrix and fiber. Both in the transverse cross section, Fig.2 (a), and in longitudinal cross section, Fig.2 (b), the interlocked fiber/matrix interface is clearly visible on both directions. The degree of interlocking is proportional to the matrix shrinkage, due to the densification phenomena, and is allowed by the anisotropic microstructure of the carbon fibers and the presence of voids between the graphene layers [13]. In fact during densification, the matrix compresses the fibers,

which plastically deform allowing the penetration of ZrB_2 grains and the formation of jagged interfaces [20]. This interface configuration results very efficient in terms of stress transfer between matrix and fiber, and does not hinder the fiber pull-out [13]. In fact, since the van der Waals bonding between the graphene layers in pitch-derived C_f is considerably weak, the interface debonding does not occur between the fiber and the matrix, but between the graphene layers within the fibers [13]. On the other hand, the strong fiber/matrix interface allows the stress build-up during the cooling step of the sintering and leaves the material in a stressed state after sintering, and homogeneously spaced cracks in the matrix with a periodicity of about *20 μm* [20]. In correspondence of the cracks both matrix and fiber release their residual stress and for that, in the following, this portion of fiber is called "inner freed fiber" (*IFF*).

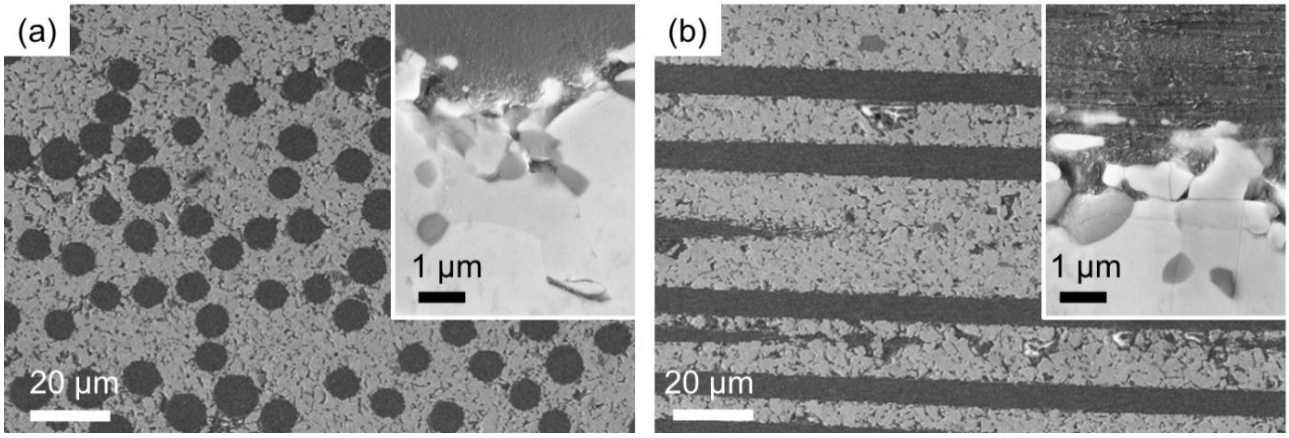

Fig.2 *SEM* micrographs of the cross section of the *UHTCMC* based on pitch-derived carbon fibers and ZrB_2/SiC matrix along (a) the transverse direction, and (b) longitudinal direction.

3.2 Thermal damage

Experimental curves in Fig.3 show the relative dimensional change ($\Delta L/L_0$) *versus* temperature up to *1300 °C* for polycrystalline ZrB_2 [21], typical anisotropic pitch-derived carbon fibers along their transverse ($C_{f,T}$) and longitudinal ($C_{f,L}$) direction [22], and unidirectional C_f-reinforced ZrB_2-matrix of this work along the transverse ($ZrB_2/C_{f,T}$) and longitudinal ($ZrB_2/C_{f,L}$) direction. All the above curves were fitted with polynomial equations and the coefficients were reported in Table 1. As expected, $\Delta L/L_0$ of the composites along *TD* and of polycrystalline ZrB_2 are very close to each other and also very comparable with that of $C_{f,T}$ (Fig.3 (a)). In

fact, the obtained *CTE* of $ZrB_2/C_{f,T}$ is intermediate between that of fiber and matrix (Table 1). The overlapping of $\Delta L/L_0$ of the composite with that of the matrix and its deviation from that of the fiber should be ascribed to the graphitic structure of the latter. In fact C_f can easily deform along the radial axis by untangling and graphitization of the graphene sheets, this avoids their elastic shrinkage along the longitudinal axis and allows that fibers plastically deform and follow the different dilation of the matrix along *TD,* where *CTE* mismatch between matrix and fiber is $-3.6 \cdot 10^{-7}$ °C^{-1}. From Fig.3 (b) it can be seen that this small *CTE* mismatch and the supposed facile plastic deformation of the fiber along TD do not affect the overall *CTE* of the composites with the succession of thermal cycles. In fact, $\Delta L/L_0$ loops are almost overlapped, and *CTE* of the composite, at the end of thermal cycling, decreased of just *0.9 %* (Table 1). On the contrary, the large linear *CTE* mismatch of $+7.3 \cdot 10^{-6}$ °C^{-1} between matrix and fiber along *LD* (Fig.3 (c)) leads to a decreasing of *52 %* the longitudinal *CTE* (from $1.75 \cdot 10^{-6}$ °C^{-1} to $0.84 \cdot 10^{-6}$ °C^{-1}, Table 1), and a permanent expansion of *0.47 %* at *RT* (Fig.3 (d)). The absolute value of the permanent expansion corresponds to *117 µm* and can be correlated to the matrix cracking which leads to the matrix shrinkage (releasing of tensile stresses) and fiber elongation (releasing of compressive stresses) along *LD*. Hence, this releasing of elastic strain leads to the formation of *IFF*.

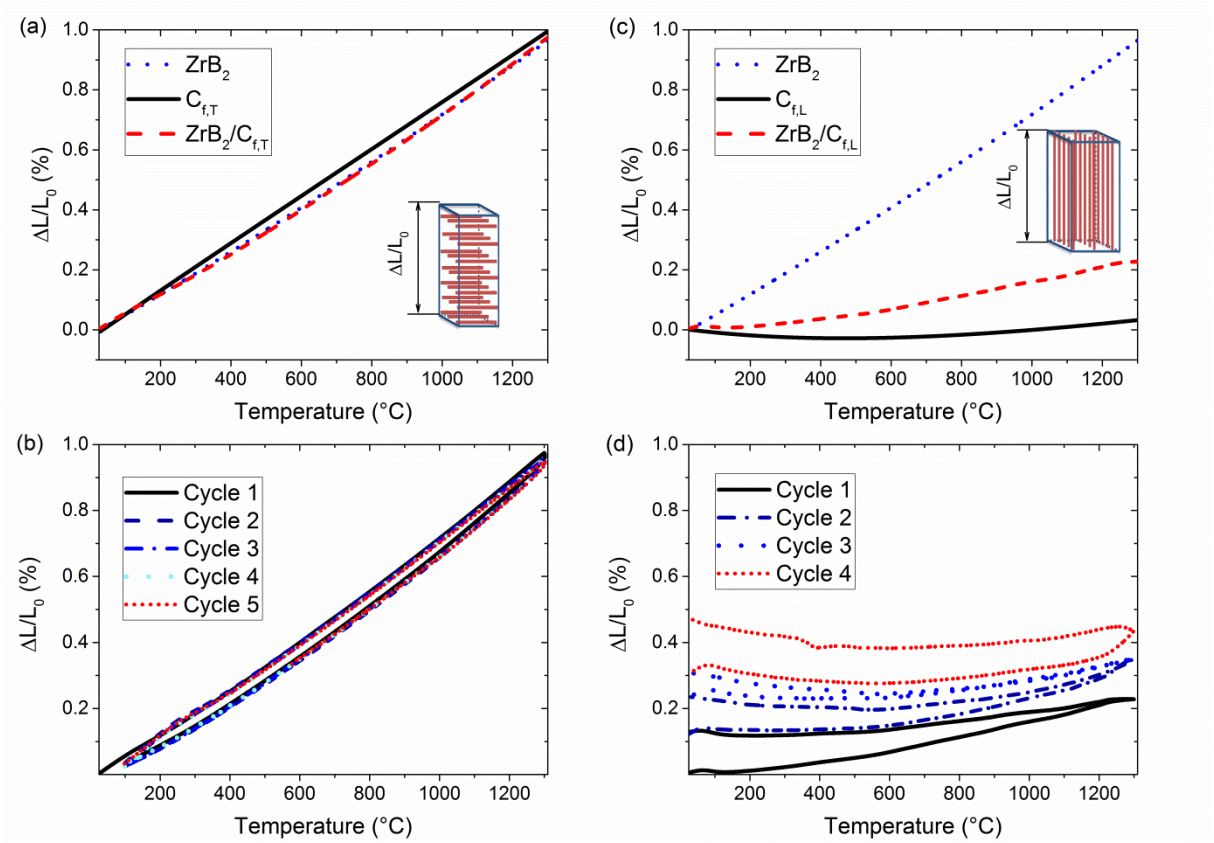

Fig.3 (a) Relative dimensional change ($\Delta L/L_0$) *vs.* temperature (T) of tested *UHTCMC* ($ZrB_2/C_{f,T}$, dashed line) along the transversal direction together with that of polycrystalline ZrB_2 [21] (dotted line), and pitch-derived fibers [22] ($C_{f,T}$, solid line) along the transversal direction. (b) Measured dilatometry curves of $ZrB_2/C_{f,T}$ during thermal cycles. (c) $\Delta L/L_0$ *vs.* T of tested *UHTCMC* ($ZrB_2/C_{f,L}$, dashed line) along the longitudinal direction together with that of polycrystalline ZrB_2 [21] (dotted line), and pitch-derived fibers [22] ($C_{f,L}$, solid line) along the longitudinal direction. (b) Measured dilatometry curves of $ZrB_2/C_{f,L}$ during thermal cycles.

Materials	#	a_4 ($°C^{-4}$)	a_3 ($°C^{-3}$)	a_2 ($°C^{-2}$)	a_1 ($°C^{-1}$)	a_0	*CTE* (10^{-6} $°C^{-1}$)	Ref.
ZrB_2	1	–	–	*6.65193E-10*	*6.69346E-6*	*-1.7922E-4*	*7.51*	–
$C_{f,T}$	1	–	*1.238E-13*	*-2.87108E-10*	*8.03756E-6*	*-2.8383E-4*	*7.87*	[22]
$C_{f,L}$	1	*1.152E-16*	*-7.35902E-13*	*2.11178E-9*	*-1.54005E-6*	*4.56636E-5*	*0.25*	[22]
$ZrB_2/C_{f,T}$	1	*-2.37084E-15*	*6.0085E-12*	*-4.10573E-9*	*8.0073E-6*	*6.39353E-5*	*7.70*	–
$ZrB_2/C_{f,T}$	5	*-2.45087E-15*	*5.94493E-12*	*-3.73478E-9*	*7.70884E-6*	*5.25088E-5*	*7.63*	–
$ZrB_2/C_{f,L}$	1	*6.55164E-16*	*-1.91583E-12*	*3.52715E-9*	*-5.23633E-7*	*1.04914E-4*	*1.75*	–
$ZrB_2/C_{f,L}$	4	*4.05192E-16*	*-3.70271E-12*	*4.44807E-9*	*-2.58827E-6*	*3.16065E-4*	*0.84*	–

Table 1 Cycles number (#). Polynomial coefficients of measured relative dimensional change ($\Delta L/L_0$): a_4, a_3, a_2,a_1, and a_0. Secant CTE in selected temperature range of 25-1300 °C.

3.3 Indentation damage

In order to study the indentation damage, *10 kg* Vickers imprints were made onto the in fiber's plane (first column of Fig.4) and out-of-fiber's plane (second column of Fig.4) of both as produced (*AP*, Fig.4 a,b) and thermally cycled (*TC*, Fig.4 c,d) specimens.

3.3.1 Indentation onto the fiber's plane

From the indentation obtained onto the fiber's plane (Fig.4 a,c), material pile-up can be seen. Indeed, during the loading, fibers are forced to bend until they break and release their compression state and producing a widespread pile-up. The pile-up height of *AP* is higher than that of *TC* (Fig.4 e). This result is in agreement with the expected initial residual stress level. In fact, since *TC* should has released its residual stress by matrix cracking and the corresponded formation of *IFFs*, the swelling of *AP* results bigger. The pile-up term, reminiscent of metal work hardening, should intended as spring up of material outside the surface since the material inside is constrained. The pile-up propagation across the surface is larger in *TD*, where the elastic modulus of the composite, $E_{c,T}$, is smaller (*70 GPa*), on the other hand it is smaller in *LD* where

$E_{c,L}$ is higher (*230 GPa*). Looking beneath the initial surface – at the imprints left by the tip – the indentation depth (*h*) and diagonal (*d*) of *TC* are about *37 %* deeper and *25 %* larger than that of *AP* (Table 2). These differences are significant and match the significant decreasing of matrix modulus with thermal cycles, which has been estimated to decrease from ≈*200 GPa* to few tens of *GPa* after three thermal cycles up to *1300 °C* [20]. Hence, on the fiber's plane the thermal cycles decrease the material stiffness as well as its hardness. The lower *d/h* value (*r*) of both *AP* and *TC* with respect to the theoretic one and to the experimental one measured on the monolithic ZrB_2-based ceramic [23] is due to the higher elastic spring back of C_f along the *x*-axis with respect to that along *z*-axis (Table 2). In other words, the elastic spring back of the fibers, dispersed within the matrix, tends to close the imprint. The higher spring back of *TC* with respect to *AP* ($r_{TC\text{-}ZrB_2/C_{f,T}} < r_{AP\text{-}ZrB_2/C_{f,T}}$, Table 2) could be due to the higher amount of *IFF*. $r_{ZrB_2}$of *9.8* is in agreement with that can be extrapolated from the Berkovich nanoindentation on ZrB_2 ceramic grains by Csanádia *et al.* [24]. In fact, considering that Berkovich indenter gives the same projected area-to-depth ratio as the Vickers indenter and that the projected areas of loaded and unloaded imprint are the same, the h/h_{max} ratio of *0.62* corresponds to a $r_{ZrB_2}$of *11.3* [24,25]. The higher value extrapolated from the nanoindentation (*11.3 > 9.8*) could be ascribed to a more elastic response of the single ZrB_2 grain with respect to that of polycrystalline area, which could improve the plastic deformation. In Fig.4 e the theoretical Vickers's imprints is drawn with the same depth of experimental ones in order (i) to better visualize the *xy* shrinkage of the experimental imprints, and (ii) to resume the parallelism with the pile-up of the metals, which is large only when $h = h_{max}$ [26].

3.3.2 Indentation onto the out-of-fiber's plane

From the characteristics of imprints into the out-of-fiber's plane (Table 2), it can be noted that *r*-values are higher than *7*. This reverse result, with respect to that obtained into fiber's plane, is due to the C_f spring back which this time acts along the *z*-axis. Also on the out-of-fiber's plane, as for fiber's plane, the spring back is bigger for the *TC* specimens ($r_{TC\text{-}ZrB_2/C_{f,L}} > r_{AP\text{-}ZrB_2/C_{f,L}}$) owing to the higher amount of *IFF*. If we consider r_{ZrB_2}instead of $r_{Th.}$, we can note that $r_{AP\text{-}ZrB_2/C_{f,L}}$ is smaller than this reference, while $r_{TC\text{-}ZrB_2/C_{f,L}}$ is larger. $r_{AP\text{-}}$

$r_{ZrB_2/C_{f,L}} < r_{ZrB_2}$ could be ascribed to the damage induced by the indenter in the stressed *AP* specimens. $r_{TC\text{-}ZrB_2/C_{f,L}} > r_{ZrB_2}$ can be justified considering that the *IFFs* can be easily buckled under the loading, hence permit a deeper penetration, and then release a larger spring back. In Fig.4 f, it can be seen that the unloaded profile of *TC* specimen has a flatter shape and almost loses that of the Vickers' indenter. As for the *AP* specimen the induced damages may free some fiber from the matrix clamping. As consequence we found the appearance of fibers outside the area of imprint (out-of-plane freed fibers, *OFF*) visible in Fig.4 b,f. This phenomenon can be described as a sort of "button effect" or "antipull-out", since occurs by pushing in. To better characterize the indentation profiles on the out-of-fiber's plane, *5* cycles of loading-unloading indentation were performed. In this way, the elastic recovery of both *IFF* and *OFF* was suppressed by destroying the free fibers (Fig.4 f) and the calculated *r*-values match that of monolithic ZrB_2.

Materials	Load (kg)	*h* (µm)	*d* (µm)	*r = d/h*
AP-$ZrB_2/C_{f,T}$	*10*	*30 ± 5*	*156 ± 6*	*5.2*
AP-$ZrB_2/C_{f,L}$	*10*	*24 ± 1*	*207 ± 17*	*8.6*
AP-$ZrB_2/C_{f,L}$ (reloaded x5)	*10*	*24 ± 1*	*235 ± 8*	*9.9*
TC-$ZrB_2/C_{f,T}$	*10*	*41 ± 4*	*195 ± 21*	*4.8*
TC-$ZrB_2/C_{f,L}$	*10*	*24 ± 3*	*311 ± 12*	*13*
TC-$ZrB_2/C_{f,L}$ (reloaded x5)	*10*	*41 ± 2*	*356 ± 14*	*9*
Monolithic ZrB_2	*1*	*2.9 ± 0*	*28.3 ± 1.1*	*9.8*
Theoretical Vickers imprint	-	*1*	*7*	*7*

Table 2 Vickers indentation results: permanent depth (*h*) and diagonals (*d*) beneath the fiber's plane ($ZrB_2/C_{f,T}$) and out-of-fiber's plane ($ZrB_2/C_{f,L}$) in as-produced (*AP*) and thermally cycled (*TC*) composites, and monolithic ZrB_2.

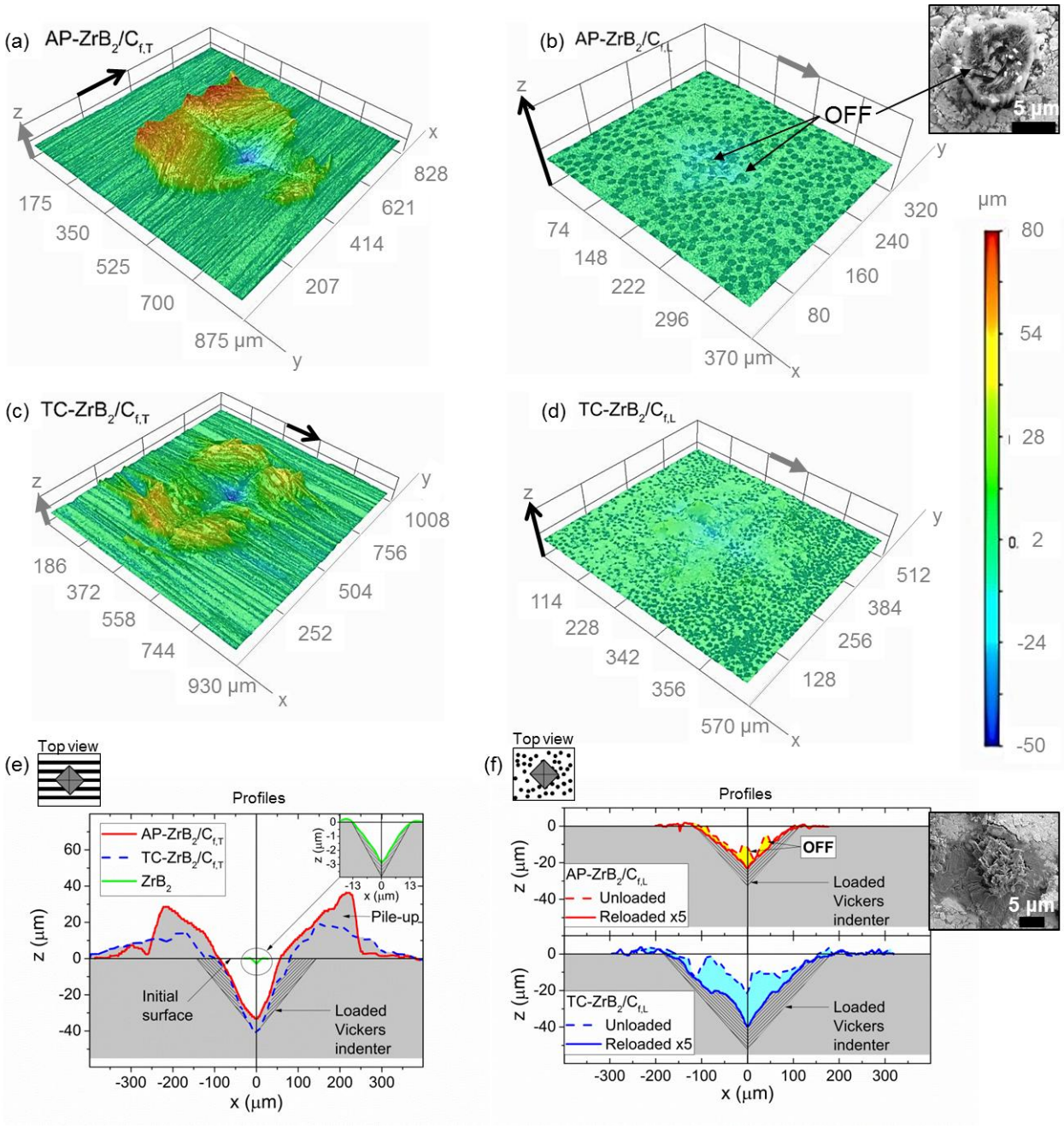

Fig.4 3D colored map of As-Produced, *AP*, (a,b) and Thermally Cycled, *TC*, (c,d) specimens indented onto fiber's plane (first column) and out-of-fiber's plane (second column). The gray and black arrows indicate the stacking direction of the yarns, and the longitudinal direction of the fibers, respectively. Red and blue colors indicate the higher and the lower height, respectively. The four 3D maps have the same *z*-scale and the initial surfaces are at the same level: *z ≈ 0 µm*. (b-inset) SEM of out-of-plane fibers (*OFF*). (e) Typical profile of the diagonal impression made on fiber's plane of *AP* (red solid line) and TC specimens (blue dashed line), and monolithic ZrB_2-based ceramic (black solid area close to the origin axes). (f) Typical profiles of the

indenter's diagonal made on out-of-fiber's plane of *AP* (dashed line in the upper plot) and *TC* specimens (dashed line in the lower plot), and after five load-unload cycles (solid lines). In all the profile plots, the horizontal axis intercepting *y = 0* and represents the initial surface. The areas filled with lines pattern represents the theoretical profile of the Vickers indenter at the maximum load of *10 kg*. (f-inset) *SEM* of out-of-plane fibers (*OFF*) after five loading-unloading cycles. (For interpretation of the references to colour in this figure legend, the reader is referred to the Web version of this article.)

3.4 Retained fracture strength after thermal cycling

After thermal cycling from *RT* to *1300°C* for *5* times, the retained strength was measured and compared to the pristine one (Fig.5 (a)). Despite the damage introduced by thermal treatments decreased the matrix elastic modulus as shown in earlier studies [20], the strength does not undergo appreciable variation, starting from *63 ±7 MPa* and remaining *62 ± 24 MPa*. Generally, when monolithic ceramics are subjected to a thermal damage, they show a retained average strength lower than *30 %* of the pristine value, and an increase of data dispersion [27,28]. In our case, since the orientation angle of fibers to the tensile direction is *90 °*, specimens were tested in matrix-dominated loading configuration where C_f act more as long defective channels, rather than reinforcing phase. Hence, both *AP* and *TC* $ZrB_2/C_{f,T}$ samples can be considered as bulk ZrB_2 materials affected by a *45 %* of anisotropic porous channels. This observation leads to justify the obtained *σ* values which are similar to that of other porous ceramics with similar architecture [29]. The reason of the higher *σ* values and damage tolerance with respect to the correspondent isotropic porous ceramics is generally ascribed to the higher tensile strength of the larger struts, and to the crack tip blunting due to the circular shape of fibers section [29,30].

Moreover, these results give a different perspective to the concept of damage tolerance. In fact, if along the longitudinal direction it is mainly the matrix porosity that enables the damage tolerance by reducing the interlaminar shear strength as a consequence of the lower matrix and matrix/fiber interface strengths [31,32], along the transverse direction it is the inverse: fibers, acting as pores, enable the damage tolerance of the dense matrix characterized by strong fiber/matrix interfaces. In the context of off-axis composite

strength and damage tolerance, such aging treatment has not detrimental effect, as well as the high matrix density and the strong interfaces.

Looking at the fracture surface of *AP* specimen (Fig.5 (b,c)), it can be seen that failure occurred mainly through the matrix and was accompanied by delamination between orthogonal yarns and fiber "scissoring", but with minimal fiber fracture. Fiber scissoring is maximized where the fracture occurred in the plane orthogonal to the yarns and transversal to the fiber axis (Fig.5 (b)). In this surface, crack tip blunting is clearly visible. The same toughening mechanism was observed for *TC* specimens (not shown). This observation supports what is surmised above: in both cases (*AP* and *TC*) the off-axis damage tolerant behaviour is not yielded by the fibers in itself, but should be ascribed to the blunting effect produced by the "channels" produced by the fibers. The fracture surface of *TC* specimen (Fig.5 (d)) displays a combination of fiber "scissoring" and "ripping". Furthermore, its matrix cracks appear wider than that of *AP* specimen. These observations attest to lower efficacy of the *TC* matrix, with respect to the *AP* matrix, in intensifying stress concentrations around fiber breaks. Anyway in both cases interlaminar shear failure was not observed (i.e. *H*-crack formation), in agreement with the designed failure (Eq.(1)), and the expected matrix-dominated loading behaviour guaranteed by the dense-matrix.

3.5 Retained fracture strength after Vickers indentation

Through Vickers indentation of *20 kg*, a damage of *50 µm* depth was introduced. The damaged specimens (labeled with *I*) gave the fracture strength, *84 ± 20 MPa* which could appear higher than that of *AP* specimens (*63 ± 7 MPa*). This feature is somewhat misleading in the sense that fracture did not started from the flaw, but quite far (*≈1 mm*) from that, and hence the indentation imprint does not act as critical defect. Hence, the composite displays a damage insensitivity [33]. The reason of this unexpected result could be the releasing of tensile stress of the matrix and the consecutive strengthening of the volume involved by the process zone (estimated to be *≈ 1 mm*^{3}). Thus, the volume from which fracture-initiation can take place should be reduced of about *20 %*. This value, all approximations aside, is a relevant part and

not a fraction, and, according to the Weibull statistics, can justifies the apparent increase of the fracture strength and the broadening of the dispersion.

For sake of comparison in Fig.5, the stress-displacement curve for a typical monolithic ZrB_2 + *10 vol%* SiC [23] is shown together with that obtained after *2 kg* indentation (*5 μm* depth) [34]. The monolithic ceramic with a retains about *24 %* of the pristine strength (from *637 ± 80 MPa* to *156 ± 11 MPa*) [23,34]. The strength retention improves when ceramics are reinforced. For example, by reinforcing Al_2O_3 with *30 vol%* SiC whisker instead of nano-sized SiC particles, the retained strength, after a Vickers imprint of about *50 μm* depth, increases from *48 %* to *72 %*. In any case, the found notch insensitivity is particularly striking: the fibers aligned along *TD* cannot bridge the crack walls and the strength drop should be comparable with that of the particulate composite [35], instead of remaining unchanged. The reason could be that nor the transverse dimension of the fibres (*10 μm*) neither the indentation damage (*50 μm*) are the critical flaw size, but the latter could consist in multiple transverse fiber sections linked by matrix cracking (*> 50 μm*). This explanation is not fully convincing since, contrary to the result presented in 3.4 section, the critical flaw size and/or density should increase with the thermal damage and decrease the transverse strength. Anyway, the retention of the off-axis strength after thermal damaging or indentation suggests that not only *UHTCMCs* can bear thermal cycles, thermal gradient, vibrations, debris impacts, etc. but also, if we look to the ratio of transverse to longitudinal strengths, $\sigma_T/\sigma_L = 0.18$ ($\sigma_T = 65$ *MPa*, $\sigma_L = 360$ *MPa*), that carbon fiber-reinforced dense *UHTCs* can bear the transverse load without need cross-ply architecture. In fact, this baseline *UHTCMCs* show a transverse strength and strength isotropy more than three times higher than that of conventional non-woven *CMCs* (σ_T = *3-20 MPa*, σ_T/σ_L = *0.004-0.029 MPa*, respectively [36-38]).

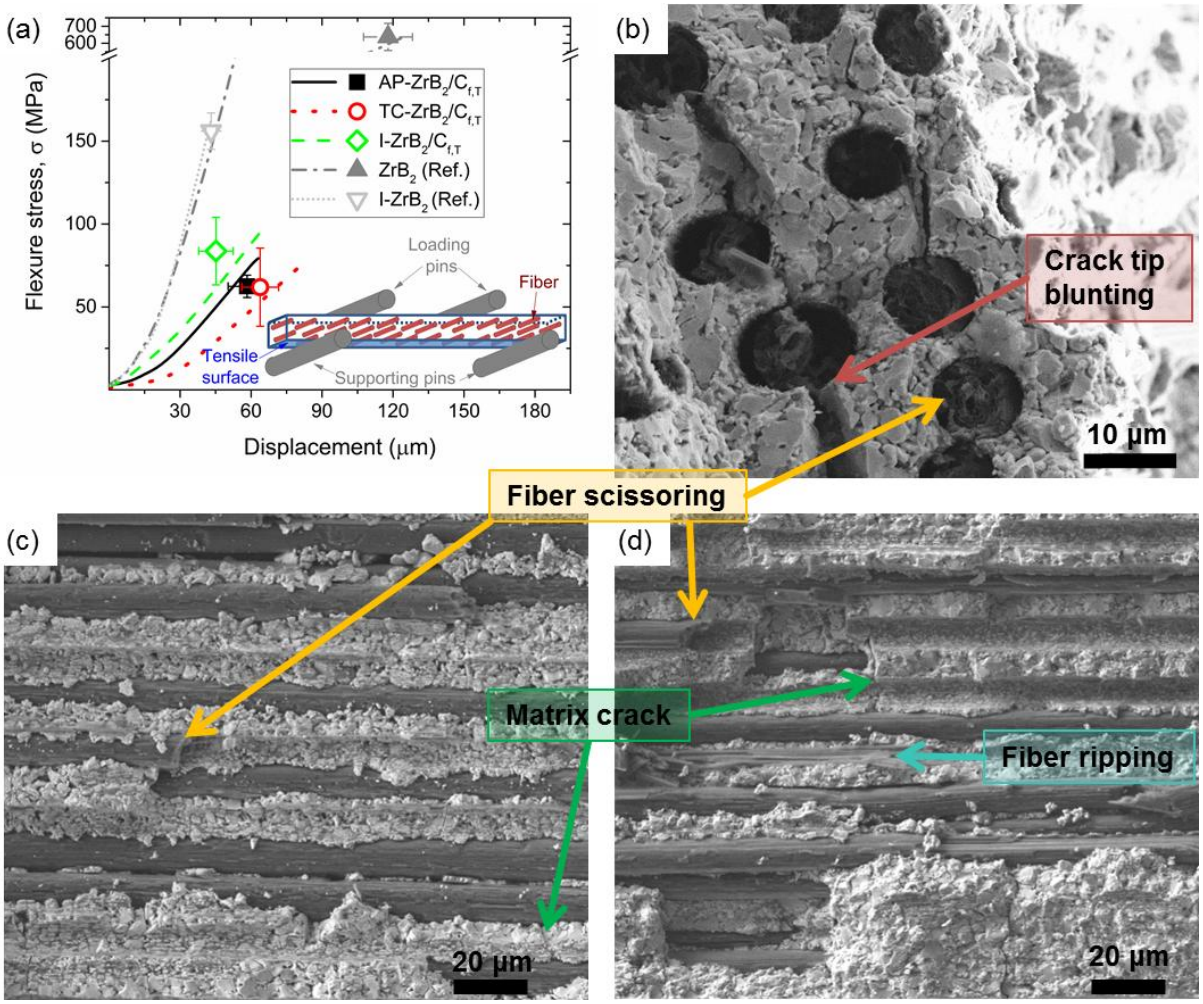

Fig.5 (a) Typical flexure stress *vs.* crosshead displacement curves obtained with a *4*-point bending test for the as produced specimens (*AP-$ZrB_2/C_{f,T}$*: solid line, and monolithic ZrB_2 [15]: dash-dotted line), thermally cycled specimens (*TC-$ZrB_2/C_{f,T}$*, dotted line), intended specimens on the tensile surface (*I-$ZrB_2/C_{f,T}$*: dashed line, indented monolithic *I-ZrB_2* [29]: short dotted line). The symbols (solid square for *AP-$ZrB_2/C_{f,T}$*, open circle for *TC-$ZrB_2/C_{f,T}$*, open diamond for *I-$ZrB_2/C_{f,T}$*, solid up triangle for ZrB_2, and open down triangle for *I-ZrB_2* [29]) represent the mean values of the fracture strength at breaking displacement. *SEM* of fracture surfaces along (b) the thickness-for-length surface and (c) thickness-for-width surfaces of as produced specimen, and (d) along thickness-for-width surfaces of thermally cycled specimen. An example of crack tip blunting, fiber scissoring, fiber ripping, and matrix crack is pointed by an arrow in each electron micrograph.

4 Conclusions

The strength retention of ultra-high temperature ceramic matrix composites (*UHTCMCs*) based on ZrB_2-matrix reinforced with *45 vol%* of unidirectional continuous carbon fibers was investigated after inducing thermal and indentation damage. The results proved that *UHTCMCs* kept their load bearing capability in both cases, and showed damage insensitivity although tested in fully matrix-dominated loading configuration (off-axis configuration). The retention of off-axis properties after thermal damaging and indentation suggested that *UHTCMCs* can bear thermal cycles, thermal gradient, vibrations, debris impacts, etc., and really can lead to a breakthrough in the aerospace field. Furthermore, thermal damage accumulation and decrease of residual stresses did not affect the coefficient of thermal expansion along the transverse direction. On the other side, thermal damage led i) to a deeper imprint, and ii) to a larger elastic recovery owing to the larger amount of inner freed fiber.

Acknowledgments

The research leading to these results has received funding from the European Union's Horizon 2020 Programme under grant agreement C3HARME No. 685594. The authors are grateful to A.N. Murri for thermal dilatometric measurements.

References

[1] L. Zoli, A. Vinci, P. Galizia, C. Melandri, D. Sciti, On the thermal shock resistance and mechanical properties of novel unidirectional UHTCMCs for extreme environments, Sci. Rep. 8 (2018) 9148. https://doi.org/10.1038/s41598-018-27328-x

[2] N.P. Padture, Advanced structural ceramics in aerospace propulsion, Nat. Mater. 15 (2016) 804–809. https://doi.org/10.1038/nmat4687

[3] D. Sciti, L. Zoli, L. Silvestroni, A. Cecere, G.D. Di Martino, R. Savino, Design, fabrication and high velocity oxy-fuel torch tests of a C_f-ZrB_2- fiber nozzle to evaluate its potential in rocket motors, Mater. Des. 109 (2016) 709–717. https://doi.org/10.1016/j.matdes.2016.07.090

[4] S. Vorotilo, K. Sidnov, I. Yu. Mosyagin, A.V. Khvan, E.A. Levashov, E.I. Patsera, I.A. Abrikosov, *Ab-initio* modeling and experimental investigation of properties of ultra-high temperature solid solutions $Ta_xZr_{1-x}C$, J. All. Comp. 778 (2019) 480-486. https://doi.org/10.1016/j.jallcom.2018.11.219

[5] J. Zou, H.-B. Ma, L. Chen, Y.-J. Wang, G.-J. Zhang, Key issues on the reactive sintering of ZrB_2 ceramics from elementary raw materials; Scr. Mater. 164 (2019) 105–109. https://doi.org/10.1016/j.scriptamat.2019.01.044

[6] E.P. Simonenko, N. P. Simonenko, A. N. Gordeev, A. F. Kolesnikov, V. G. Sevastyanov,N. T. Kuznetsov, Behavior of HfB_2–30 vol% SiC UHTC obtained by sol–gel approach in the supersonic airflow, J. Sol-Gel Sci. Technol. (2019). https://doi.org/10.1007/s10971-019-05029-9

[7] K. Kavakeb, Z. Balak, H. Kafashan, Densification and flexural strength of ZrB_2–30 vol% SiC with different amount of HfB_2, Int. J. Refract. Met. H. 83 (2019) 104971. https://doi.org/10.1016/j.ijrmhm.2019.104971

[8] S. Karimirad, Z. Balak, Characteristics of spark plasma sintered ZrB_2-SiC-SCFs composites, Ceram. Int. 45 (2019) 6275–6281. https://doi.org/10.1016/j.ceramint.2018.12.109

[9] S. Failla, P. Galizia, L. Zoli, A. Vinci, D. Sciti, Toughening effect of non-periodic fiber distribution on crack propagation energy of UHTC composite, J. All. Comp. 777 (2018) 612-618. https://doi.org/10.1016/j.jallcom.2018.11.043

[10] P. Hu, D. Zhang, S. Dong, Q. Qu, X. Zhang, A novel vibration-assisted slurry impregnation to fabricate C_f/ZrB_2-SiC composite with enhanced mechanical properties, J. Eur. Ceram. Soc. 39 (2018) 798-805. https://doi.org/10.1016/j.jeurceramsoc.2018.10.029

[11] D. Zhang, P. Hu, S. Dong, Q. Qu, X. Zhang, Effect of pyrolytic carbon coating on the microstructure and fracture behavior of the C_f/ZrB_2-SiC composite, Ceram. Int. 44 (2018) 19612-19618. https://doi.org/10.1016/j.ceramint.2018.07.210

[12] C. Fang, P. Hu, S. Dong, P. Xie, K. Wang, X. Zhang, Design and optimization of the coating fibers and sintering temperature for ZrB_2-SiC-C_f composites prepared by hot pressing, J Eur. Ceram. Soc 39 (2019) 2805-2811. https://doi.org/10.1016/j.jeurceramsoc.2019.03.038

[13] P. Galizia, S. Failla, L. Zoli, D. Sciti, Tough salami-inspired C_f/ZrB_2 UHTCMCs produced by electrophoretic deposition, J. Eur. Ceram. Soc. 38 (2018) 403–409. https://doi.org/10.1016/j.jeurceramsoc.2017.09.047

[14] H. Hu, Q. Wang, Z. Chen, C. Zhang, Y. Zhang, J. Wang, Preparation and characterization of C/SiC–ZrB_2 composites by precursor infiltration and pyrolysis process, Ceram. Int. 36 (2010) 1011–1016. https://doi.org/10.1016/j.ceramint.2009.11.015

[15] W.-C. Tu, F.F. Lange, A.G. Evans, Concept for a damage-tolerant ceramic composite with "strong" interfaces, J. Am. Ceram. Soc. 79:2 (1996) 417-24. https://doi.org/10.1111/j.1151-2916.1996.tb08138.x

[16] E.A.V. Carelli, Effects of thermal aging on the mechanical properties of a porous-matrix ceramic composite, J. Am. Ceram. Soc. 85:3 (2002) 595-602. https://doi.org/10.1111/j.1151-2916.2002.tb00138.x

[17] G.-J. Zhang, J.-F. Yang, T. Ohji, Fabrication of porous ceramics with unidirectionally aligned continuous pores, J. Am. Ceram. Soc. 84:6 (2001) 1395-1397. https://doi.org/10.1111/j.1151-2916.2001.tb00849.x

[18] J.A. Heathcote, X.-Y. Gong, J.Y. Yang, U. Ramamurty, F.W. Zok, In-plane mechanical properties of an all-oxide ceramic composite, J. Am. Ceram. Soc. 82 [10] (1999) 2721-30. https://doi.org/10.1111/j.1151-2916.1999.tb02148.x

[19] F.W. Zok, C.G. Levi, Mechanical properties of porous-matrix ceramic composites, Adv. Eng. Mater. 3 (2001) 15-23. https://doi.org/10.1002/1527-2648(200101)3:1/2<15::AID-ADEM15>3.0.CO;2-A

[20] P. Galizia, L. Zoli, D. Sciti, Impact of residual stress on thermal damage accumulation, and Young's modulus of fiber-reinforced ultra-high temperature ceramics, Mater. Des. 160 (2018) 803-809. https://doi.org/10.1016/j.matdes.2018.10.019

[21] F. Monteverde, S. Guicciardi, A. Bellosi, Advances in microstructure and mechanical properties of zirconium diboride based ceramics, Mater. Sci. Eng. A 346 (2003) 310–319. https://doi.org/10.1016/S0921-5093(02)00520-8

[22] C. Pradere, C. Sauder, Transverse and longitudinal coefficient of thermal expansion of carbon fibers at high temperatures (300–2500 K), Carbon 46 (2008) 1874–1884. https://doi.org/10.1016/j.carbon.2008.07.035

[23] F. Monteverde, S. Guicciardi, C. Melandri, D. Dalle fabbriche, Densification, Microstructure Evolution and Mechanical Properties of Ultrafine SiC Particle-Dispersed ZrB_2 Matrix Composites. In: Orlovskaya N., Lugovy M. (Eds.), Boron Rich Solids, NATO Science for Peace and Security Series B: Physics and Biophysics. Springer, Dordrecht, 2010, pp. 261-272. https://doi.org/10.1007/978-90-481-9818-4_17

[24] T. Csanádia, A. Kovalčíková, J. Dusza, W.G. Fahrenholtz, G.E. Hilmas, Slip activation controlled nanohardness anisotropy of ZrB_2ceramicgrains, Acta Mater. 140 (2017) 452-464. https://doi.org/10.1016/j.actamat.2017.08.061

[25] W.C. Oliver, G.M. Pharr, Measurement of hardness and elastic modulus by instrumented indentation: advances in understanding and refinements to methodology, J. Mater. Res.19:1 (2004) 3-20. https://doi.org/10.1557/jmr.2004.19.1.3

[26] E. Broitman, Indentation hardness measurements at macro-, micro-, and nanoscale: a critical overview, Tribol. Lett. 65:23 (2017) 1-18. https://doi.org/10.1007/s11249-016-0805-5

[27] F. Monteverde, L. Scatteia, Resistance to thermal shock and to oxidation of metal diborides-SiC ceramics for aerospace application, J. Am. Ceram. Soc. 90, 1130–1138 (2007). https://doi.org/10.1111/j.1551-2916.2007.01589.x

[28] W. Zhi, Q. Qiang, W. Zhanjun, S. Guodong, The thermal shock resistance of the ZrB_2-SiC–ZrC ceramic, Mat. Des. 32 (2011) 3499–3503. https://doi.org/10.1016/j.matdes.2011.02.056

[29] J. Cao, Z. Lu, K. Miao, H. Zhao, Y. Xia, F. Wang, B. Lu, Fabrication of high-strength porous SiC-based composites with unidirectional channels, J. Am. Ceram. Soc. (2019) 1–11. https://doi.org/10.1111/jace.16332

[30] C. Tallon, C. Chuanuwatanakul, D.E. Dunstan, G.V Franks. Mechanical strength and damage tolerance of highly porous alumina ceramics produced from sintered particle stabilized foams, Ceram. Int. 42 (2016) 8478–8487. https://doi.org/10.1016/j.ceramint.2016.02.069

[31] M.A. Mattoni, J.Y. Yang, C.G. Levi, F.W. Zok, Effects of matrix porosity on the mechanical properties of a porous-matrix, all-oxide ceramic composites, J. Am. Ceram. Soc. 84:11 (2001) 2594-602. https://doi.org/10.1111/j.1151-2916.2001.tb01059.x

[32] O. Ševeček, L. Bertolla, Z. Chlup, L. Řehořek, Z. Majer, P. Marcián, M. Kotoul, Modelling of cracking of the ceramic foam specimen with a central notch under the tensile load, Theor. Appl. Fract. Mec. 100 (2019) 242-250. https://doi.org/10.1016/j.tafmec.2019.01.024

[33] F. Tavangarian, D. Hui, G. Li, Crack-healing in ceramics. Compos. Part B-Eng. 144 (2018) 56-87. https://doi.org/10.1016/j.compositesb.2018.02.025

[34] F. Saraga, F. Monteverde, Self-healing ability of ultra high temperature ceramics, in : L. Silvestroni, C. Galassi, E. Di Bartolomeo, M. Dondi (Eds.), Proceedings of the first workshop for young ceramists, Novembre 26-27, 2018, Bologna, Italy. La Mandragora s.r.l.

[35] T. Osada, N. Wataru, K. Takahashi, K. Ando, Self-crack-healing behavior in ceramic matrix composites, in I.M. Low (Eds.), Advances in Ceramic Matrix Composites, Woodhead Publishing Series in Composites Science and Engineering, 2014, pp. 410-441. https://doi.org/10.1016/B978-0-08-102166-8.00021-9

[36] R. Bhatt, R Phillips, Laminate behavior for SiC fiber-reinforced reaction-bonded silicon nitride matrix composites, J. Comps. Technol. Res. 12: 1 (1990) 13-23. https://doi.org/10.1520/CTR10173J

[37] J. Koyanagi, H. Hatta, M. Kotani, H. Kawada, A Comprehensive Model for Determining Tensile Strengths of Various Unidirectional Composites, J. Compos. Mater. 43:18 (2009) 1901-1914. https://doi.org/10.1177/0021998309341847

[38] D. Zhang, D.R. Hayhurst, Stress–strain and fracture behaviour of 0°/90°and plain weave ceramic matrix composites from tow multi-axial properties, Int. J. Solids Struct. 47 (2010) 2958-2969. https://doi.org/10.1016/j.ijsolstr.2010.06.023

Graphical Abstract

Click here to download high resolution image